# Noise reduction method using a variance map of the phase differences in digital holographic microscopy


doi: https://doi.org/10.4218/etrij.2021-0311

Received: 28 September 2021 | Revised: 6 December 2021 | Accepted: 28 December 2021

DOI: 10.4218/etrij.2021-0311

ORIGINAL ARTICLE

ETRI Journal WILEY

# Noise reduction method using a variance map of the phase differences in digital holographic microscopy

**Hyun-Woo Kim**[1] | **Myungjin Cho**[2] | **Min-Chul Lee**[1]

[1]Department of Computer Science and Networks, Kyushu Institute of Technology, Iizuka-shi, Fukuoka, Japan

[2]School of ICT, Robotics, and Mechanical Engineering, IITC, Hankyong National University, Anseong, Republic of Korea

**Correspondence**
Myungjin Cho, School of ICT, Robotics, and Mechanical Engineering, IITC, Hankyong National University, Anseong, Republic of Korea.
Email: mjcho@hknu.ac.kr

Min-Chul Lee, Department of Computer Science and Networks, Kyushu Institute of Technology, Iizuka-shi, Fukuoka, Japan.
Email: lee@csn.kyutech.ac.jp

**Funding information**
Ministry of Education, Grant/Award Number: NRF-2017K1A3A1A19070753

**Abstract**

The phase reconstruction process in digital holographic microscopy involves a trade-off between the phase error and the high-spatial-frequency components. In this reconstruction process, if the narrow region of the sideband is windowed in the Fourier domain, the phase error from the DC component will be reduced, but the high-spatial-frequency components will be lost. However, if the wide region is windowed, the 3D profile will include the high-spatial-frequency components, but the phase error will increase. To solve this trade-off, we propose the high-variance pixel averaging method, which uses the variance map of the reconstructed depth profiles of the windowed sidebands of different sizes in the Fourier domain to classify the phase error and the high-spatial-frequency components. Our proposed method calculates the average of the high-variance pixels because they include the noise from the DC component. In addition, for the nonaveraged pixels, the reconstructed phase data created by the spatial frequency components of the widest window are used to include the high-spatial-frequency components. We explain the mathematical algorithm of our proposed method and compare it with conventional methods to verify its advantages.

**KEYWORDS**
digital holographic microscopy, noise reduction, three-dimensional imaging

## 1 | INTRODUCTION

The phase information of light cannot be obtained directly using human eyes and image sensors because they can only detect the intensity of light. To obtain the phase information of light, one needs to obtain the interference characteristics of the light used by a coherent light source. Holography [1] is a representative technique that uses coherence to obtain the phase information of light. In this technique, reference and object beams are generated using coherent plane waves or spherical waves, and the interference pattern between them is recorded on a photosensitive plate or an image sensor. When the object beam is scattered by objects, the phase information and interference pattern change. This altered interference pattern provides the shape information of the object, and the three-dimensional (3D) shape information of the object can be obtained using holography. Digital holography (DH) [2] has the same principle as holography but uses image sensors instead of films for recording. DH has been widely applied in many applications, such as 3D image encryption [3,4], 3D image recognition [5–7], digital holographic reconstruction [8,9], and digital holographic microscopy (DHM) [10–26].

DHM is used for disease diagnosis [19,25], 3D profiling of microstructures [12,22], and microbial research [10,16,21,24] because it can reconstruct the thickness profile of micro-objects with a high depth resolution. In DHM reconstruction, a sideband (corresponding to the object information) in the Fourier domain is windowed to obtain the specimen thickness. In this process, when a wide window is used, high-spatial-frequency components are included. Thus, the detailed thickness information of the specimen can be obtained. However, this information also has noise from the DC component in the Fourier domain, leading to phase error. Therefore, when a wide-windowed sideband is used, the high-spatial-frequency components of the specimen are included, but the phase error increases. However, when a narrow window is used, the phase error decreases, but the high-spatial-frequency components of the specimen are lost. Moreover, when the DHM interferometry changes, the sideband position also changes, thereby altering the distance between the DC component and the sideband. Therefore, a trade-off exists between the sideband window size and the phase error. This noise can be reduced using conventional filtering methods, such as Gaussian and median filtering. These conventional approaches use the height information of the neighboring pixels of the target pixel. Hence, many researchers have been studying filtering methods for DHM using spatial filtering [27,28], spiral phase filters [29], and deep learning techniques [30], among others.

In this paper, we propose a phase-error reduction method for DHM called high-variance pixel averaging (HiVA), which can address the above issue. We compare the noise reduction effectiveness of HiVA with that of conventional filtering methods using an unfiltered specimen height profile.

The remainder of this paper is organized as follows. In Section 2, we explain the principles of DHM and HiVA. Section 3 presents a description of the experimental setup and conditions. In Section 4, we provide the experimental results and the results of the comparison of our proposed method with the conventional filtering methods. Finally, in Section 5, we discuss the effectiveness of HiVA based on the experimental results.

## 2 | THEORY

### 2.1 | Phase error in the processing of DHM

In DHM, the image sensor can record only the intensity of the hologram. This intensity information can be expressed as follows [15,22]:

$$\mathrm{Hol} = |R|^2 + |O|^2 + R^* O + RO^*, \tag{1}$$

where Hol is the hologram intensity recorded by the image sensor; $R$ and $O$ are the complex amplitudes of the reference and object beams, respectively; the $|R|^2 + |O|^2$ term is the DC component; and the $R^* O + RO^*$ term represents the positive and negative sidebands in the Fourier domain. $A^*$ is the complex conjugate of $A$. This equation can be derived as follows:

$$\mathrm{Hol} = I_R + I_O + R^* O e^{j(\phi_O - \phi_R)} + RO^* e^{-j(\phi_O - \phi_R)}, \tag{2}$$

where $\phi_O$ and $\phi_R$ are the phase information of the object and reference beams, respectively, and $\phi_O - \phi_R$ is the phase difference between the object and reference holograms. This phase difference can be represented by $\Delta\phi$, and the depth information of the specimen can be obtained from $\Delta\phi$ using the following equation [15, 22]:

$$\Delta\phi(x,y) = \frac{\omega}{c}(n_s - n_m)h(x,y), \tag{3}$$

$$h(x,y) = \frac{\Delta\phi(x,y)}{K \times \Delta n}, \tag{4}$$

where $K = \omega/c, \Delta n = n_s - n_m, \omega$ is the angular frequency, $c$ is the speed of light, and $n_s$ and $n_m$ are the constant refractive indices of the specimen and the surrounding medium, respectively. $h$ is the height information of the specimen, $K$ is the wavenumber, and $\Delta n$ is the difference of the refractive index.

Figure 1 shows the interference pattern of a recorded hologram and its Fourier domain [22]. Specifically, Figure 1A is the spatial domain, and Figure 1B is the spatial frequency domain. In Figure 1B, the positive or negative sidebands are shown on both sides of the DC component, and a circle can be drawn to illustrate the overlap between the DC component and the sidebands.

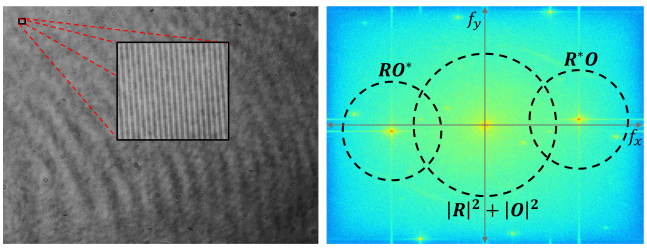


(A) (B)

FIGURE 1 (A) Interference pattern of the recorded hologram and (B) Fourier domain of the hologram

However, the DC component is also distributed weakly and widely in the high-spatial-frequency region. These sidebands have the spatial frequency components of the object. Thus, a sideband is windowed for the DHM reconstruction process. When a wide sideband window is used, the high-spatial-frequency components of the object are reconstructed, but the phase error and the information of the DC component also increase. In contrast, when a narrow sideband window is used, the phase error decreases, but the high-spatial-frequency components of the object are lost. Therefore, we propose HiVA.

## 2.2 | HiVA

HiVA windows the two-dimensional spatial frequency domain of both the reference and object holograms from the narrow region to the wide one at regular intervals, then creates a variance map using phase reconstruction. Thus, we can calculate the average of the high-variance pixels because they include the noise from the DC component. In addition, for the nonaveraged pixels, the reconstructed phase data created by the spatial frequency components of the widest window are used. HiVA can be expressed as follows:

$$S(x,y) = \frac{1}{N_\mathrm{d}} \times \sum_{i=1}^{N_\mathrm{d}} \frac{\Delta\phi_i(x,y)}{K \times \Delta n}, \tag{5}$$

$$V(x,y) = \frac{1}{N_\mathrm{d}} \times \sum_{i=1}^{N_\mathrm{d}} \left\{ \frac{\Delta\phi_i(x,y)}{K \times \Delta n} - S(x,y) \right\}^2, \tag{6}$$

$$h_\mathrm{HiVA}(x,y) = \begin{cases} \dfrac{\Delta\phi_{N_\mathrm{d}}(x,y)}{K \times \Delta n}, & V(x,y) < m_\mathrm{V}, \\ \dfrac{1}{N_\mathrm{d}} \times \displaystyle\sum_{i=1}^{N_d} \dfrac{\Delta\phi_i(x,y)}{K \times \Delta n}, & V(x,y) \geq m_V, \end{cases} \tag{7}$$

where $S$ and $V$ are the average and variance, respectively, of the height information of the specimen; $m_\mathrm{V}$ is the average of the variance $V$; and $N_\mathrm{d}$ is the number of phase reconstruction data for various sizes of the windowed sideband. The average of the variance $m_\mathrm{V}$ is used as the threshold value for segmenting the high-variance pixels and the other pixels in (7). We performed an optical experiment to verify the effectiveness of HiVA.

# 3 | EXPERIMENTAL SETUP

By using a modified Mach–Zehnder interferometer with two spherical waves to make the fringe pattern as narrow as possible, we cropped the spatial frequency sidebands to make them as wide as possible and thus include the high-spatial-frequency components of the specimen.

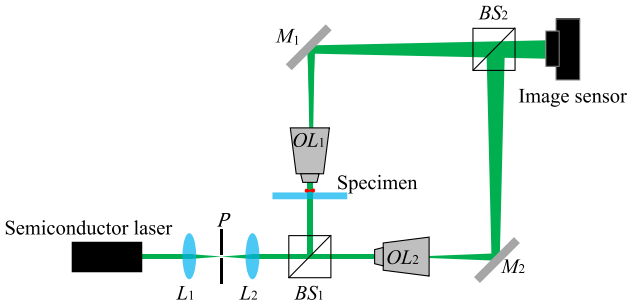


FIGURE 2 Experimental setup. *L*: lens, *P*: pinhole, *M*: mirror, *BS*: beam splitter, and *OL*: objective lens

Figure 2 illustrates the experimental setup used to verify the effectiveness of HiVA. It included a semiconductor laser diode module (532-nm wavelength and 3-mW output power) with a collimating setup. $L_1$ was a 10 × objective lens, and $L_2$ was a collimating lens. The diameter of the laser through $L_2$ was 2 mm. Thin red blood cell (RBC) smears from healthy males were used as the specimens. The object and reference beams were magnified by 40 × (0.65 NA) objective lenses. To record the hologram, we used a CMOS sensor (Basler acA2500-14uc) with a pixel resolution of 2590 (H) × 1942 (V) and a pixel size of 2.2 μm (H) × 2.2 μm (V).

# 4 | EXPERIMENTAL RESULTS

## 4.1 | Modification of the equations

Figure 3 shows the experimental results obtained by HiVA. Figure 3A,B demonstrates the acquired image using the DHM experimental setup with the RBCs and the phase differences of Figure 3A, respectively. These phase difference data were obtained by the widest window. Figure 3C,D demonstrates a variance map of all the reconstructed depth data and the result of the zero replacement of pixels lower than the threshold value of Figure 3C, respectively. Thus, only the filtering pixels are shown in Figure 3D. However, we changed the algorithm because the difference between the maximum value and the other values in the variance map was too large to be segmented using the threshold value. Figure 3E,F demonstrates the logarithm of the variance map and the result of the zero replacement of pixels lower than the threshold value of Figure 3E, respectively. As shown in Figure 3E, the high variances were mostly located at the specimen boundaries. Therefore, we modified (7) as follows:

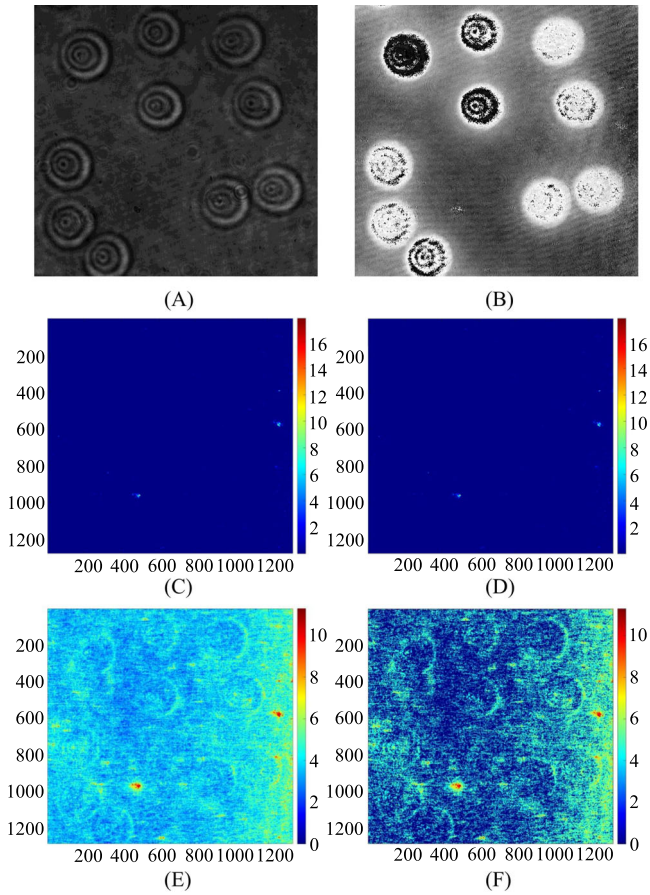


FIGURE 3 (A) Recorded hologram image, (B) calculated phase differences of (A), (C) variance map of all reconstructed depth data, (D) result of the zero replacement of pixels lower than the threshold value of (C), (E) logarithm of (C), and (F) result of the zero replacement of pixels lower than the threshold value of (E)

$$h_{\mathrm{HiVA}}(x,y) = \begin{cases} \dfrac{\Delta\phi_{N_\mathrm{d}}(x,y)}{K \times \Delta n}, & \log V(x,y) < m_{\mathrm{LV}}, \\ \dfrac{1}{N_\mathrm{d}} \times \displaystyle\sum_{i=1}^{N_\mathrm{d}} \dfrac{\Delta\phi_i(x,y)}{K \times \Delta n}, & \log V(x,y) \geq m_{\mathrm{LV}}. \end{cases} \tag{8}$$

In (8), we use the average of the logarithm variance map ($m_{\mathrm{LV}}$) as a new threshold value for the segmentation. In addition, all the filtering algorithms used in this study were applied after phase unwrapping.

## 4.2 | Effectiveness of the proposed method

We used the Goldstein phase unwrapping algorithm [31] to obtain a 3D profile of the specimens. In addition, the data window used for reconstruction by the proposed method was widened at intervals of 30 pixels horizontally and vertically from 90 (H) × 90 (V) pixels to 660 (H) × 660 (V) pixels. Figure 4A demonstrates the reconstructed thickness profile of the RBCs obtained by the widest windowed phase region. Moreover, Figure 4B,C demonstrates the results obtained by applying (5) and (8), respectively. As shown in Figure 4, HiVA can simultaneously reconstruct high-spatial-frequency components and remove the noise from the DC component. Therefore, HiVA is more effective for DHM. However, Figure 4B,C indicates no significant differences. For this reason, we compared the results by calculating the signal-to-noise ratio (SNR) and the mean square error (MSE) [32] as performance metrics. In the SNR and MSE processing, the phase reconstruction data of the sidebands with the narrowest windows (60 (H) × 60 (V) pixels) served as a reference for comparing only the noise coming from the DC component. In addition, for statistical comparison, we randomly selected 20 different RBCs and obtained 3D profile data from the widest windowed sidebands.

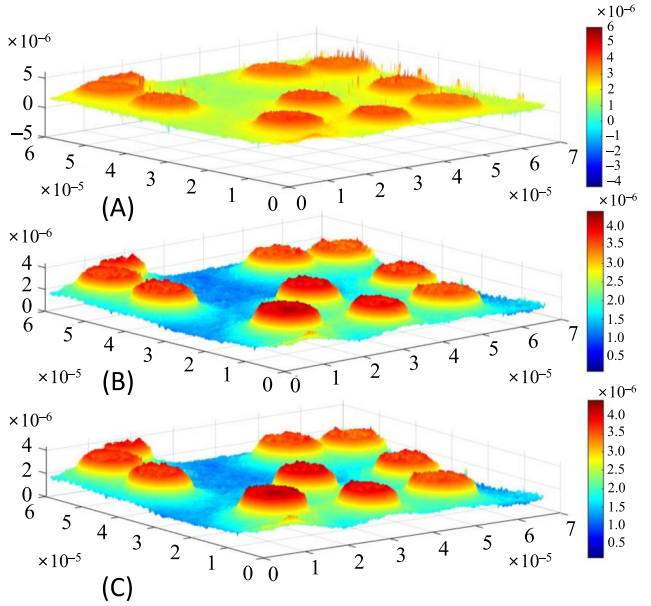


FIGURE 4 Reconstructed 3D profile by (A) the widest windowed phase region, (B) all-pixel averaging, and (C) the proposed method

Figure 5 shows the results of the SNR and MSE comparisons. In Figure 5A, the effectiveness of the conventional filtering methods (Gaussian and median filtering) and HiVA is shown. The filter size of each conventional method was modified to obtain a similar SNR/MSE ratio to that of HiVA because if the filter size were further increased, the depth information would be approximated only by the height information of the RBCs. In the case of the RBCs with serious phase errors, the conventional filtering methods could not reduce the noise, but HiVA

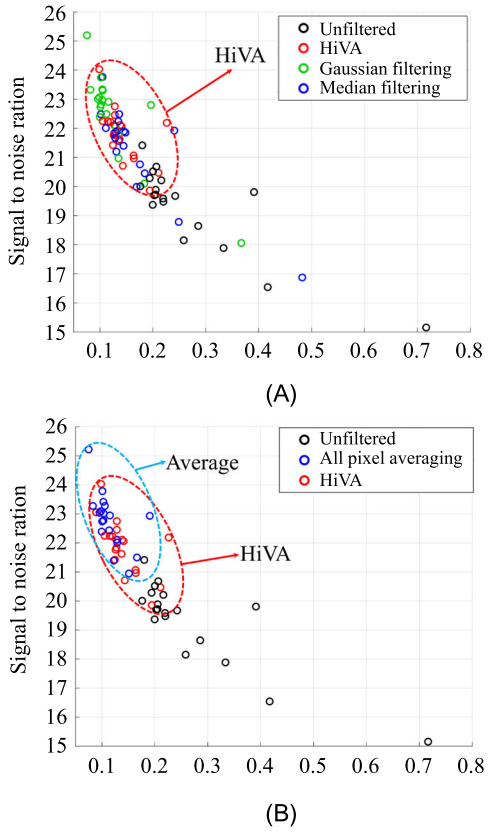


FIGURE 5 SNR and MSE comparison (A) between conventional filtering methods and the proposed method and (B) between all-pixel averaging and HiVA

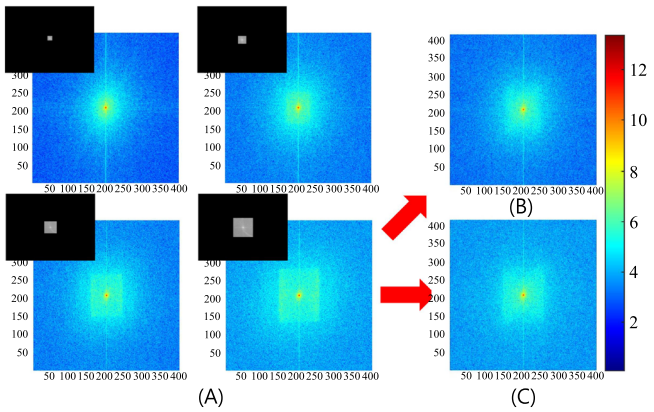


FIGURE 6 Spatial frequency domain of the reconstructed depth information with (A) each size of the windowed sideband, (B) all-pixel averaging, and (C) the proposed method

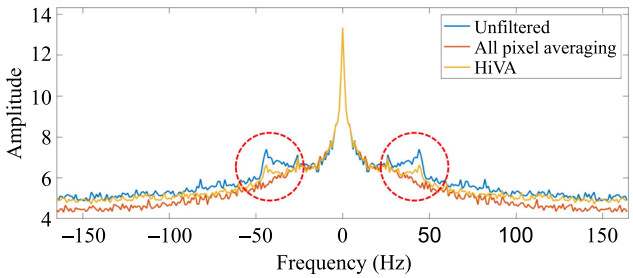


FIGURE 7 Spatial frequency domain comparison with all-pixel averaging and the proposed method using a 1D graph

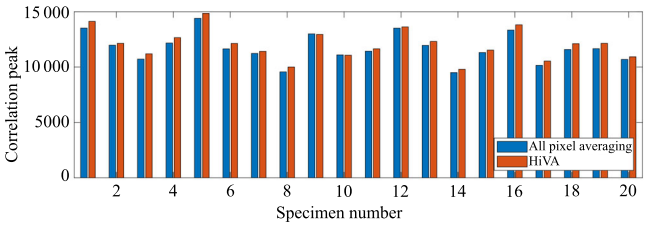


FIGURE 8 Correlation peak comparison

could. In other words, HiVA has the stability of a 3D profile. In addition, we compared the all-pixel averaging method and HiVA, as shown in Figure 5B. Both methods had stable filtering effects, but the result of the all-pixel averaging method was more stable than that of HiVA. Therefore, to show the advantage of HiVA, we compare the spatial frequency domain of the reconstructed depth data in the next section.

## 4.3 | Spatial frequency domain comparison

Figure 6 demonstrates the spatial frequency domain of the reconstructed depth information. As seen in Figure 6A, a wider window size of the sideband region was used, and a larger area of the spatial frequency components was obtained. However, the all-pixel averaging method may filter this larger area of the spatial frequency components, as shown in Figure 6B. In contrast, HiVA could maintain this larger area, as shown in Figure 6C.

Figure 7 shows a one-dimensional (1D) graph of the spatial frequency domain of the reconstructed depth information. In Figure 7, the red solid line shows all-pixel averaging and unfiltered data, the yellow solid line shows the HiVA data, and the red dotted circles indicate the areas of the specific spatial frequency components. The specific spatial frequency components of the all-pixel averaging method are weaker than those of HiVA. Again, we used 20 randomly selected RBCs and then calculated their correlation peaks [32].

Figure 8 shows a comparison of the correlation peaks of the all-pixel averaging method and HiVA with the

20 randomly selected RBCs. As shown in Figure 8, 90% of the RBCs processed by HiVA had a higher correlation peak than those of the all-pixel averaging method. Only 10% of the RBCs processed by the all-pixel averaging method had a higher correlation peak than those of HiVA. Therefore, although the simple averaging method could reduce the noise effectively and stably, it also reduced the high-spatial-frequency components. In contrast, HiVA could not only reduce the noise effectively and stably but also keep the high-spatial-frequency components.

## 5 | CONCLUSION

We propose HiVA, a new method of reducing the phase error from the DC component in DHM using a variance map of the reconstructed depth profiles of windowed sidebands of different sizes. We compared HiVA with conventional filtering methods, and the result showed that the noise reduction effectiveness of HiVA was more stable than that of the conventional approaches. In addition, we compared HiVA with the all-pixel averaging method. The effectiveness of both methods was stable, but HiVA had the advantage of preserving the high-spatial-frequency components. To verify this, we compared these approaches using the spatial frequency domain of the reconstructed depth data. The result showed that HiVA preserved the larger spatial frequency components of the wide-windowed sideband. The threshold value was used as the average of the logarithm of the variance map. This value can be modified using the median value or the average of the maximum and minimum values. HiVA can be applied to all other techniques based on DH. However, it cannot accurately classify the noise and the high-spatial-frequency components in the Fourier domain. In the future, we will investigate a method of classifying the phase error and the high-spatial-frequency components in DHM more accurately.

## ACKNOWLEDGMENT

This research was supported by Basic Science Research Program through the National Research Foundation of Korea (NRF) funded by the Ministry of Education (NRF-2017K1A3A1A19070753).

## CONFLICT OF INTEREST

The authors declare that there are no conflicts of interest.

## ORCID

*Hyun-Woo Kim* https://orcid.org/0000-0003-1381-6116
*Myungjin Cho* https://orcid.org/0000-0003-2896-770X
*Min-Chul Lee* https://orcid.org/0000-0001-8469-0288

## REFERENCES

1. D. Gabor, *A new microscopic principle*, Nature **161** (1948), 777–778.
2. P. Picart and S. Montresor, *Optical holography*, Elsevier, Amsterdam, 2020.
3. M. L. Piao, Y. L. Piao, and N. Kim, *3D image encryption based on computer-generated hologram in the fractional Fourier domain*, (Practical Holography XXXIII: Displays, Materials, and Applications, San Francisco, CA, USA), 2019. https://doi.org/10.1117/12.2509161
4. M. L. Piao, H. Y. Wu, and N. Kim, *3D image encryption based on computer-generated hologram*, (Digital Holography and Three-Dimensional Imaging, Bordeaux, France), May 2019. https://doi.org/10.1364/DH.2019.W3A.21
5. U. Abeywickrema, R. Gnawali, and P. P. Banerjee, *Identification of 3D objects using correlation of holograms*, (Proc. SPIE 10752, Applications of Digital Image Processing XLI, San Diego, SA, USA), 2018. https://doi.org/10.1117/12.2322668
6. B. Bordbar, H. Zhou, and P. P. Banerjee, *3D object recognition through processing of 2D holograms*, Appl. Opt. **58** (2019), G197–G203.
7. I. Shevkunov, V. Katkovnik, D. Claus, G. Pedrini, N. V. Petrov, and K. Egiazarian, *Spectral object recognition in hyperspectral holography with complex-domain denoising*, Sensors **19** (2019), no. 23, 5188.
8. Z. Ren, Z. Xu, and E. Y. M. Lam, *End-to-end deep learning framework for digital holographic reconstruction*, Adv. Photon. **1** (2019), no. 1, 16004.
9. H. Wang, M. Lyu, and G. Situ, *eHoloNet: a learning-based end-to-end approach for in-line digital holographic reconstruction*, Opt. Express **26** (2018), 22603–22614.
10. M. Bedrossian, C. Lindensmith, and J. L. Nadeau, *Digital holographic microscopy, a method for detection of microorganisms in plume samples from enceladus and other icy worlds*, Astrobiology **17** (2017), 913–925.
11. A. Dong, K. Yetisen, X. Dong, F. Poller, M. Jakobi, Z. Liu, F. S. Bloise, and A. W. Koch, *Low-pass filtering compensation in common-path digital holographic microscopy*, Appl. Phys. Lett. **117** (2020), no. 12, 121105.
12. L. Huang, L. Yan, and B. Chen, *Phase restoration of digital holographic microscopy with an adaptive reliability mask for phase unwrapping in microstructure testing*, Opt. Lasers Eng. **138** (2021), 106416.
13. L. Huang, L. Yan, B. Chen, Y. Zhou, and T. Yang, *Phase aberration compensation of digital holographic microscopy with curve fitting testing*, Opt. Commun. **462** (2020), 125311.
14. B. Javidi, A. Markman, S. Rawat, T. O'Connor, A. Anand, and B. Adermariam, *Sickle cell disease diagnosis based on spatio-temporal cell dynamics analysis using 3D printed shearing digital holographic microscopy*, Opt. Express **26** (2018), 13614–13627.
15. H. W. Kim, K. Inoue, M. Cho, and M. C. Lee, *A study on real-time modification of the refractive index of a surrounding medium using a uniform microsphere in digital holographic microscopy*, (EEET '20: Proceedings of the 2020 3rd International Conference on Electronics and Electrical Engineering Technology, Kitakyushu, Japan), Sept. 2020. https://doi.org/10.1145/3429536.3429539
16. J. Li, B. Li, and X. Zhang, *Digital holographic microscopy measures underwater microorganism*, (Second Target Recognition

and Artificial Intelligence Summit Forum, Changchun, China), 2020. https://doi.org/10.1117/12.2553034
17. T. O'Connor, A. Anand, and B. Javidi, *Field-portable microsphere-assisted high resolution digital holographic microscopy in compact and 3D-printed Mach-Zehnder Interferometer*, OSA Contin. **3** (2020), 1013–1020.
18. T. O'Connor, A. Doblas, and B. Javidi, *Structured illumination in compact and field-portable 3D-printed shearing digital holographic microscopy for resolution enhancement*, Opt. Lett. **44** (2019), 2326–2329.
19. N. Palacios-Ortega, M. D. S. Hernandez-Montes, F. Mendoza-Santoyo, and J. M. Flores-Moreno, *Measurement of morphology thickness and refractive index in a melanoma A375 cell line using digital holographic microscopy*, Appl. Opt. **60** (2021), 815–822.
20. N. Patel, S. Rawat, M. Joglekar, V. Chhaniwal, S. K. Dubey, T. O'Connorm, B. Javidi, and A. Anand, *Compact and low-cost instrument for digital holographic microscopy immobilized micro-particles*, Opt. Lasers Eng. **137** (2021), 106397.
21. D. Roitshtain, N. A. Turko, B. Javidi, and N. T. Shaked, *Flipping interferometry and its application for quantitative phase microscopy in a micro-channel*, Opt. Lett. **41** (2016), 2354–2357.
22. S. Shin and Y. Yu, *Fine metal mask 3-dimensional measurement by using scanning digital holographic microscope*, J. Korean Phys. Soc. **72** (2018), 863–867.
23. S. Shin and Y. Yu, *Lensless reflection digital holographic microscope with a Fresnel-Bluestein transform*, J. Korean Phys. Soc. **74** (2019), 98–101.
24. S. M. Solis, M. S. Hernandez-Montes, and F. M. Santoyo, *Identification of microorganisms using digital holographic microscopy*, (Emerging Challenges for Experimental Mechanics in Energy and Environmental Applications, Proceedings of the 5th International Symposium on Experimental Mechanics and 9th Symposium on Optics in Industry (ISEM-SOI)), 2015, pp. 71–74.
25. F. Yi, I. Moon, and Y. H. Lee, *Three-dimensional counting of morphologically normal human red blood cells via digital holographic microscopy*, J. Biomed. Opt. **20** (2015), no. 1, 16005.
26. Z. Zhong, H. Zhao, L. Cao, M. Shan, B. Liu, W. Lu, and H. Xie, *Automatic cross filtering for off-axis digital holographic microscopy*, Results Phys. **16** (2020), 102910.
27. Y. Hong, T. Shi, X. Wang, Y. Zhang, K. Chen, and G. Liao, *Weighted adaptive spatial filtering in digital holographic microscopy*, Opt. Commun. **382** (2017), 624–631.
28. J. Li, C. Dang, Y. Chen, Q. Luo, P. Zhao, J. Zhao, and C. Wang, *Adaptive spatial filtering based on fuzzy C-means and phase in off-axis digital holographic microscopy*, Opt. Eng. **60** (2021), no. 5, 51207.
29. H.-Y. Tu, W.-J. Hsiao, X.-J. Lai, Y.-C. Lin, and C.-J. Cheng, *Synthetic aperture common-path digital holographic microscopy with spiral phase filter*, J. Opt. **19** (2017), no. 6, 65604.
30. W. Xiao, Q. Wang, F. Pan, R. Cao, X. Wu, and L. Sun, *Adaptive frequency filtering based on convolutional neural networks in off-axis digital holographic microscopy*, Biomed. Opt. Express **10** (2019), no. 4, 1613–1626.
31. R. M. Goldstein, H. A. Zebker, and C. L. Werner, *Satellite radar interferometry: Two-dimensional phase unwrapping*, Radio Sci. **23** (1988), no. 4, 713–720.
32. R. C. Gonzalez and R. E. Woods, *Digital image processing*, Pearson, New York, 2018.

## AUTHOR BIOGRAPHIES

**Hyun-Woo Kim** received his B.S. from Jeju National University, Jeju, Republic of Korea, in 2011 and M.S. from Korea University, Seoul, Republic of Korea in 2015. He is currently a doctoral student at Kyushu Institute of Technology in Japan. He worked as a student researcher and a researcher at Korea Institute of Science and Technology, Republic of Korea, from 2011 to 2017. His research interests include autostereoscopic 3D display, integral imaging, DH, and DHM.

**Myungjin Cho** received his B.S. and M.S. in Telecommunication Engineering from Pukyong National University, Pusan, Republic of Korea, in 2003 and 2005, respectively, and M.S. and Ph.D. in Electrical and Computer Engineering from the University of Connecticut, Storrs, CT, USA, in 2010 and 2011, respectively. Currently, he is an associate professor at Hankyong National University, Republic of Korea. He worked as a researcher at Samsung Electronics in Republic of Korea from 2005 to 2007. His research interests include 3D display, 3D signal processing, 3D biomedical imaging, 3D photon counting imaging, 3D information security, 3D object tracking, 3D underwater imaging, DHM, photon counting, and 3D visualization of objects under inclement weather conditions.

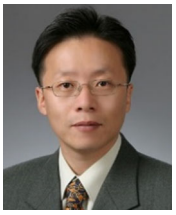

**Min-Chul Lee** received his B.S. in Telecommunication Engineering from Pukyong National University, Busan, Republic of Korea, in 1996, and his M.S. and Ph.D. from Kyushu Institute of Technology, Fukuoka, Japan, in 2000 and 2003, respectively. He is an associate professor at Kyushu Institute of Technology, Japan. His research interests include medical imaging, blood flow analysis, 3D display, 3D integral imaging, DHM, and 3D biomedical imaging.

**How to cite this article:** H.-W. Kim, M. Cho, and M.-C. Lee, *Noise reduction method using a variance map of the phase differences in digital holographic microscopy*, ETRI Journal (2022), 1–7. https://doi.org/10.4218/etrij.2021-0311